Supporting Information

Propagation length of antiferromagnetic magnons governed by domain configurations

Andrew Ross[1,2,†], Romain Lebrun[1,†,], Olena Gomonay[1], Daniel A. Grave[3], Asaf Kay[3], Lorenzo Baldrati[1], Sven Becker[1], Alireza Qaiumzadeh[4], Camilo Ulloa[5], Gerhard Jakob[1,2], Florian Kronast[6], Jairo Sinova[1,7], Rembert Duine[4,5,8], Arne Brataas[4], Avner Rothschild[3], Mathias Kläui[1,2,4,*]*

[1]Institut für Physik, Johannes Gutenberg Universität-Mainz, 55099, Mainz, Germany.

[2]Graduate School of Excellence Materials Science in Mainz (MAINZ), Staudinger Weg 9, 55128, Mainz, Germany.

[3]Department of Materials Science and Engineering, Technion-Israel Institute of Technology, Haifa 32000, Israel.

[4]Center for Quantum Spintronics, Department of Physics, Norwegian University of Science and Technology, NO-7491 Trondheim, Norway.

[5]Institute for Theoretical Physics, Utrecht University, Princetonplein 5, 3584 CC Utrecht, The Netherlands.

[6]Helmholtz-Zentrum Berlin für Materialien und Energie, Albert-Einstein-Strasse 15, D-12489 Berlin, Germany.

[7]Institute of Physics ASCR, Cukrovarnicka 10, 162 53 Praha 6 Czech Republic.

[8]Department of Applied Physics, Eindhoven University of Technology, P.O. Box 513, 5600 MB Eindhoven, The Netherlands.

1. Sample Preparation and Characterization

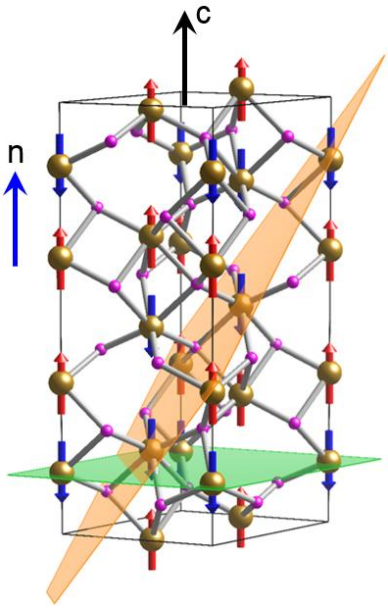

Supplemental Figure. S1. The magnet moments lie parallel to the crystallographic c-axis, the same axis that the DMI vector lies along and is the easy-axis of the antiferromagnetic structure. The two planes of interest are shown: the (0001) plane is indicated in green and the $(1\bar{1}02)$ plane in orange.[1]

All films were grown on sapphire substrates of different orientations in order to facilitate the growth of the desired hematite films. The films were deposited as previously described[2] from a stoichiometric target of Fe_2O_3 by pulsed laser deposition in an oxygen atmosphere with a substrate set point temperature of 800 °C. Hematite crystallizes in the so-called corundum structure consisting of a hexagonal *ab* basal plane extended along the *c*-axis. The corundum structure is also that of sapphire, a common insulating substrate that is used here. The unit cell of hematite below the Morin transition is shown in Supplemental Fig. S1 with the two planes of interest indicated.

The films were characterized by both X-Ray diffraction (XRD) and superconducting quantum interference magnetometry measurements (SQUID). Supplemental Figs. S2 and S3 of the Supplementary Information show the characterization for the (0001) and $(1\bar{1}02)$ films repesctively. For the SQUID measurements, the films were saturated with 3 T at the starting temperature and then were cooled at a constant rate of 2 K/min under a static applied field ranging from 10 mT to 500 mT depending on the sample. The sample was then warmed in the same field at a rate of 5 K/min. Due to the

diamagnetic contribution to the signal from the sapphire substrates used to grow the films, a constant subtraction to the signal was made from the data from the average value of the magnetization below the observed transition.

For the non-local transport measurements, wires were defined using electron beam lithography and the subsequent lift-off of 7 nm of Pt deposited in an Ar atmosphere in a chamber with a base pressure of $2x10^{-9}$ mbar. After deposition of the Pt, the wires were contacted using a bilayer of Cr (4nm)/ Au (32 nm). The center-to-center separations were varied from 425 nm to 5.5 μm. The wire widths were 250 nm with a parallel length of 80 μm for center-to-center separations up to 1 μm. For separations greater than this, a parallel length of 160 μm was used to increase the signal to noise ratio and decrease the geometric impact on the measured signal. In order to allow for direct comparison between the two geometries, calibration distances of 500 nm were used in both geometries. The samples were mounted to a piezo-rotating element installed into the variable temperature insert of a superconducting magnet. Transport measurements were performed at 175 K for the (0001) and $(1\bar{1}02)$ hematite films. The piezo-rotating element allows for 300° of continuous rotation, thus for rotation measurements, the sample was rotated in a static field for 200°. The field was then inverted and the sample rotated back to 0° allowing for a full 360° rotation with a large overlap between the forward and backward rotations. For uniaxial measurements, the angle was fixed while the field was swept along one of the three primary axes. A Keithley 2400 source meter was used to provide the injection current with a magnitude of I_{inj}=±600 μA ($3.43x10^{11}$ A/m^2) whilst the resulting non-local voltage was read-out by a Keithley 2182A nanovoltmeter.

The magnetic properties of the hematite films were further investigated by means of X-ray photo-emission electron microscopy (X-PEEM). These measurements were carried out at the SPEEM endstation of the UE49_PGM beamline at the BESSY-II synchrotron source of the Helmholtz-Zentrum Berlin.

To investigate the two films, we capped them with 2 nm of Pt to prevent the building up of charge at the insulating surface and acquired x-ray absorption spectra (XAS) at the Fe L2,3 edges. The spectra were

acquired either using linear vertical (LV) or linear horizontal (LH) polarization. The X-ray Magnetic Linear Dichroism (XMLD) is calculated according to the formula:

$$XLMD = \frac{LV - LH}{LV + LH}$$

Here, the linear vertical polarization is the in-plane polarization.

1.1 Sample Characterization for hematite (0001)

Samples grown on (0001) sapphire lead to a similar alignment of the hematite film. A 100 nm film was grown in this orientation and the out of plane crystallinity was investigated by X-ray diffraction (XRD), as shown in Supplemental Fig. S2(a).

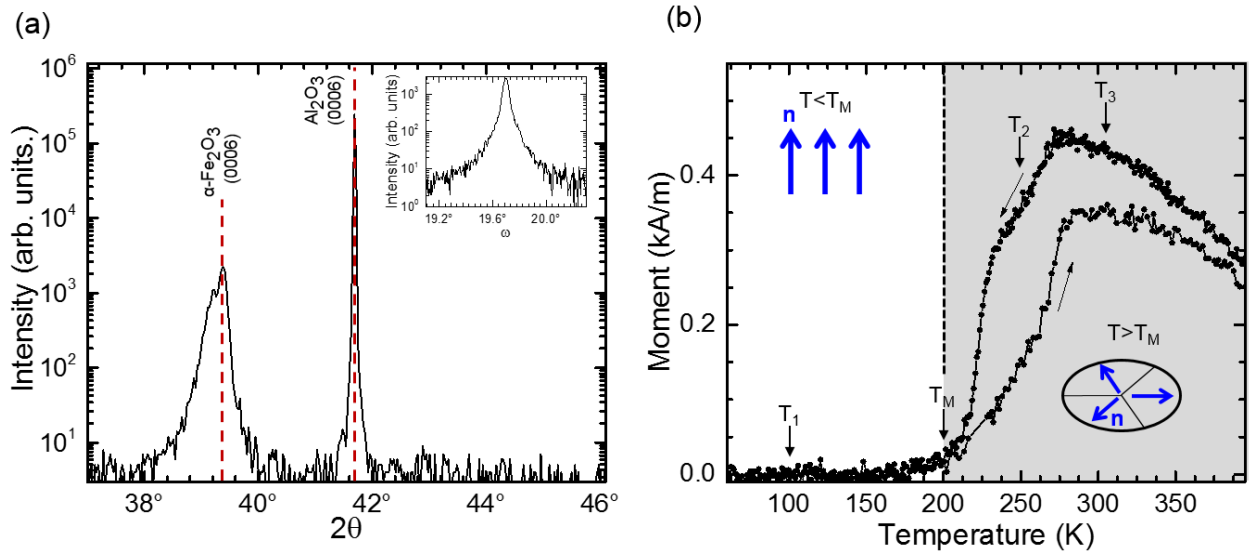

Supplemental Figure. S2. (a) XRD scan of (0001) hematite grown on sapphire. The (0006) peak of both hematite and sapphire are clearly visible and indicated. Insert: Rocking curve of (0006) peak. b) Temperature dependence of the magnetization for the film shown in (a). At 300 K, the existence of a canted moment leads to a measurable magnetization that decreases with temperature before becoming constant around zero at 200 K which is attributed to the Morin temperature of this film. The temperatures indicated as T_1, T_2 and T_3 are those where the XMLD-PEEM images of Fig. 4a-4**c** of the main text have been taken.

The alignment of the crystallites was further checked by performing a rocking curve where the value of 2θ is kept constant whilst the ω angle is varied around the expected value, insert of Supplemental Fig. S2(a). From the XRD and rocking curve, we can say that the growth of the films is epitaxial, however, the peak value for ω from the rocking curve differs from that expected from the 2θ measurement. This arises from the fact that the XRD measurements are performed by aligning to the substrate peak on the assumption that the film and substrate are aligned parallel. The shift in the value of ω leads us to the conclusion that there is a slight tilting of the hematite unit cell away from the *c*-axis of the substrate. Furthermore, from the finite width of the rocking curve, we can conclude that there is a distribution of the growth direction as a result of crystallites. Finally, in the (0006) peak of the film, there is a small shoulder indicating the existence of a second length scale of the out of plane lattice constant within the film. Collectively, these slight off axis components give rise to the PEEM contrast visible in the main text below the Morin transition due to a distribution of the Néel vector orientation as well as acting as points of defect and strain, allowing for the nucleation of domains [3]. The magnetization was measured via SQUID magnetometry as shown in Supplemental Fig. S2(b). This measurement was performed by cooling at a constant rate in an external magnetic field of 100 mT applied in the plane of the sample, perpendicular to the *c*-axis of the film. The magnetization increases slightly as we cool from 400 K to 300 K and the magnetic state is in the easy-plane phase as shown in the sketch of Supplemental Fig. S2(b). As the temperature decreases further, the magnetization begins to decrease until it becomes constant around zero at 200 K, with the complete transition taking place across 50 K. We attribute this temperature to the complete rotation of the spin structure along the *c*-axis and label it as the Morin temperature T_M [4]. As we increase the temperature again, the magnetization increases as the spin structure

returns to the easy plane phase. The Morin transition in our thin film displays a large thermal hysteresis, an effect previously reported in literature for thin films and nanoparticles of hematite [5,6]. The XMLD-PEEM images of this sample, Fig. 4(a)-4(c) of the main text, were recorded at T_1, T_2 and T_3 as indicated on Fig. S2b.

1.2 Sample Characterization for hematite $(1\bar{1}02)$

The 500 nm film of hematite was grown on sapphire $(1\bar{1}02)$ substrates in order to have the sample surface being the $(1\bar{1}02)$ plane, known as the r-plane. Supplemental Fig. S3(a) shows the XRD across the $(1\bar{1}02)$ peak for this film with the rocking curve being presented in the inset. The broad rocking curve indicates that there is a distribution in the unit cell growth directions as well as the peak for the rocking curve occurring at a value slightly smaller than expected from the XRD 2θ measurement, indicating that the growth direction of the film does not follow exactly the substrate direction. XRD scans across the (0006) and $(11\bar{2}0)$ peaks of the film and substrate allow for the extraction of both the *c*- and *a*-axis lattice constants to be $c = 13.718$ Å and $a = 5.0196$ Å which are slightly smaller than the bulk values. Supplemental Fig. S3(b) shows a reciprocal space map of the *c*-axis of the film and substrate. The *c*-axis of the film is parallel to the substrate meaning that if we apply a magnetic field along the direction of the substrate *c*-axis, then this is also along the hematite *c*-axis.

The temperature dependence of the magnetization is shown in Supplemental Fig. S3(c), where a clear Morin transition is observed when cooled under 10 mT, with minimal thermal hysteresis. The Morin temperature can be assigned to be around 200 K, slightly reduced from bulk. The transition also takes place across a large temperature range. Both the reduction, even in such a thick film, and the broad transition can both be attributed to the smaller unit cell of the film as compared to the bulk values leading to a change in the temperature dependence of the competing anisotropies that underlie the physics of the Morin transition [7].

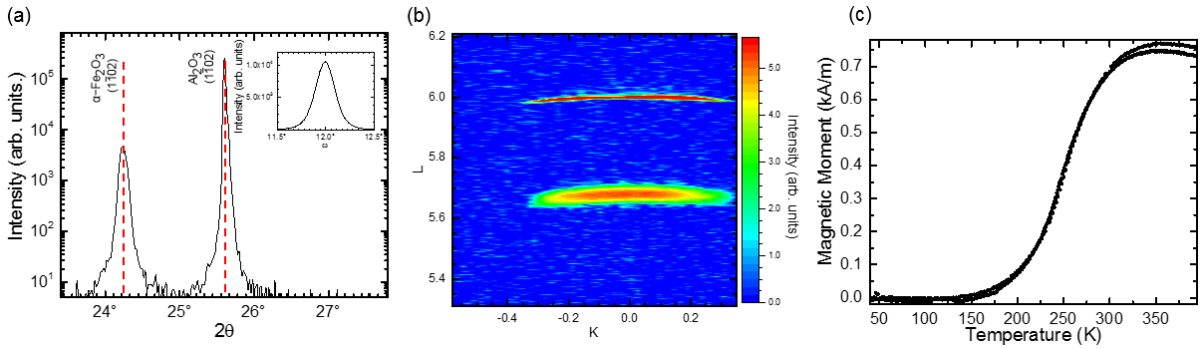

Supplemental Fig. S3: Characterization of (1$\bar{1}$02) oriented hematite films *(a) XRD of* (1$\bar{1}$02) *film showing the* (1$\bar{1}$02) *peak of both hematite and the sapphire substrate. Inset: Rocking curve of the hematite* (1$\bar{1}$02) *peak. (b) Reciprocal space map around the* (0006) *substrate peak showing the alignment of the film and substrate. (c) Temperature dependence magnetization measured by SQUID showing a Morin transition at* T = 200 K.

2. Angular Dependence of (0001) Film

In order to investigate the angular dependence of R_{el}, the (0001) film was rotated in a static field in the *xy* plane. This dependency is shown in Supplemental Fig. S4(b) as a function of angle where α is the angle between the applied field and the injection current and indicated in Supplemental Fig. S4(a). A parallel alignment of **H** and I_{inj} occurs for α = 0°. The shape of R_{el} shows a $\cos^2\alpha$ dependence with a maximal signal for the field applied along the wire. This is different to ferromagnets where a maximum signal occurs for a perpendicular alignment of **H** and I_{inj} [8]. This further supports the claim that the magnon current originating from the spin-bias is carried by the Néel order of the antiferromagnet and requires a parallel alignment of $\boldsymbol{n}$ and $\boldsymbol{\mu_s}$ [9]**.** The signal increase with field until a peak is reached at $\mu_0 H$ = 2.6 T before being suppressed at higher fields, confirming the uniaxial measurements shown in the main text. For symmetry between the signal for **H** parallel or antiparallel to the wire also supports the lack of an observation of a hysteresis in the uniaxial measurements.

Alongside rotation within the **xy** plane, where the spin-bias signal is either carried by the Néel order and maximal at $H_{c,DMI}^{\perp}$ and zero for **H**||**y**, rotation in the **yz** plane was also carried out. This would then rotate between the field applied along the easy axis, out of the plane, and in plane, perpendicular to the wire

and the easy axis. The spin-bias signal for this plane of rotation is shown in Supplemental Fig. S4(c) for static fields of varying magnitudes. At low and high fields, the signal is small with little distinct variations, as expected from looking at the uniaxial scans in the main text Figs. 1(b) and 1(c). At 4.5 T, a significant shape appears where the signal is zero for **H**||**y** (β=90°) and diverges for **H**||**z** (β = 180°). Between these two angles, the signal adopts a smoother shape, as expected from the spin reorientations observed in hematite previously. For a field parallel within a few degrees of the easy axis, here **z**, the spin transition is an abrupt spin flop, whilst for any angle off axis, it adopts a smoother, second order like transition [10]. The shape of this field scan further confirms that the spin-bias signal is carried entirely by the Néel order of an easy axis antiferromagnet. For fields away from the spin-flop field, there a smooth transition that is suppressed as **H** approaches the easy axis.

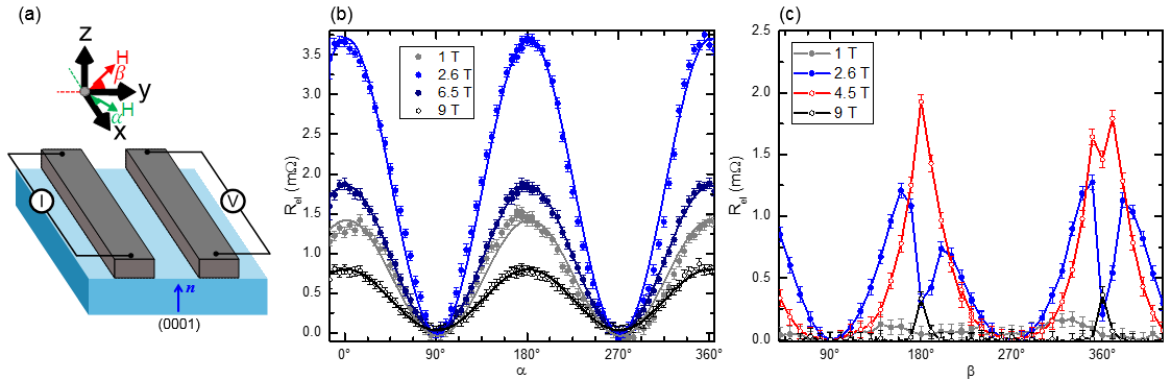

Supplemental Figure S4. (a) Non-local schematic with coordinate system and Néel vector orientation indicated. The angle between **x** and **y** is α where H||**x** is at α=0°. The angle between **y** and **z** is denoted as β where H||**z** is β=0°. (b) R_{el} for rotation in the α plane for different static fields. The shape is characteristic of a $\cos^2$ due to the cos dependence picked up by both injection and detection of magnons. (c) Beta plane scan of the non-local transport. The smooth rotation between the axes diverges for H||**z** when the critical field is reached and suppressed for other fields.

3. Temperature dependence of the transport signal in (0001) orientated films

In this section, the transport signals for a magnetic field parallel (**H**//***z***) or perpendicular (**H**//***x***) to the easy-axis in (0001) orientated films at 100 K and 295 K are presented. Supplemental figure S5 shows R_{el} at 100 K for both field directions whilst Supplemental Figure S6 shows the same for 295 K. The shape of the signals at 100 K is similar to that shown in the main text Figures 1b) and 1c), where for **H**//***x*** there is again no hysteresis but the critical field $H_{c,DMI}^{\perp}$ is shifted slightly to higher fields as expected from measurements of the temperature dependence of the critical fields in hematite.[10] The magnitude of the signal is also suppressed at the reduced temperature, an effect previously reported for non-local magnon transport in ferrimagnetic insulators given the reduction of the thermal magnon population at these reduced temperatures. [11] For **H**//***z*** the critical field for both the increasing and decreasing magnetic field are increased, again due to the complex temperature dependence of the critical anisotropies in hematite reducing the critical fields at higher temepratures.[10] The signal is again suppressed by the reduced temperature, however far more drastically that for **H**//***x***. Whilst the curves presented in Fig. 1b) of the main text were taken on a device with 500 nm wire separation, that of Supplemental Fig. 5b) was taken on a device with 200 nm of wire separation. A detailed discussion of the temperature dependence of the spin diffusion lengths of the two geometries is however beyond the scope of this manuscript.

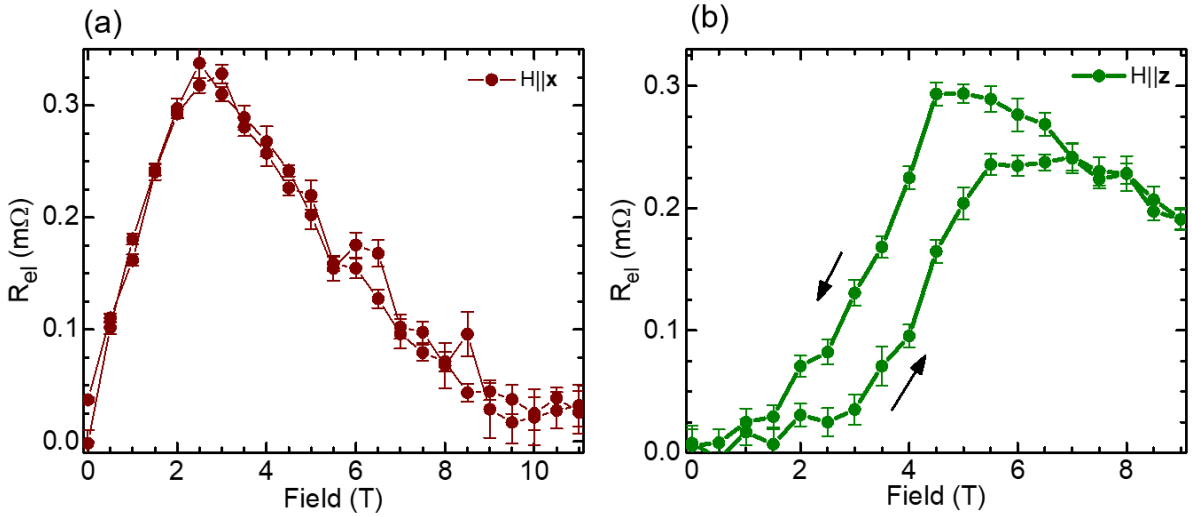

Supplemental Figure S5 Non-local transport on 100 nm thick (0001) hematite films at 100 K for a field applied (a) perpendicular and (b) parallel to the easy-axis. The device in (a) has a wire separation of 500 nm whilst that in (b) is 200 nm.

When warming above the Morin transitions, the films become less insulating, as shown in supplemental figure 6a and b at 295 K. At this temperature the films are in the easy-plane phase and transport should be limited by the polarisation of the magnon modes. The large offset makes it challenging to resolve any possible magnon transport so we perform also rotational measurements in the *xz* plane, shown in supplemental figure 6c. At low magnetic fields, there is no evidence of modulation as a function of angle, however at large magnetic fields, some periodicity begins to enter. However a full investigation of the magnon transport in this phase, where the less insulating nature allows other effects such as anisotropic magnetoresistance to enter, alongside the role of the canted moment and its effects on the magnon polarisation[12] is beyond the scope of this work.

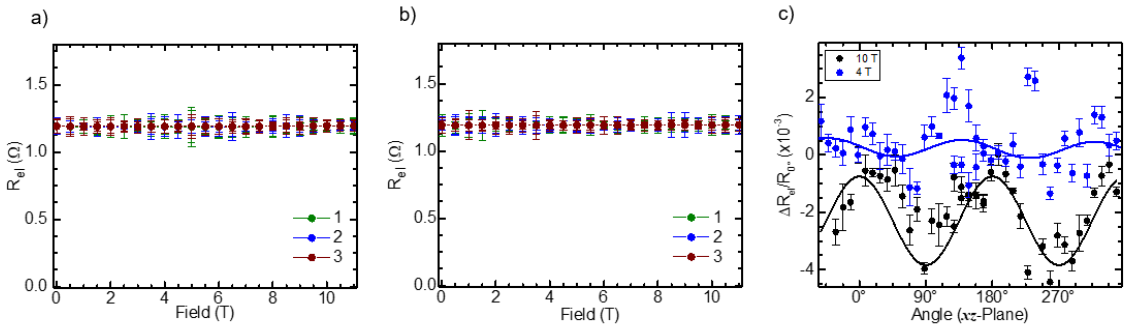

Supplemental Figure S6 Non-local transport on 100 nm thick (0001) hematite films at 295 K for a field applied a) perpendicular and b) parallel to the easy-axis. The devices in both have a wire separation of 500 nm and become less insulating at high temperatures. c) Angular dependence of the same device in the xz plane at μ_0H = 4 (blue) and 10 (black) T normalised by the value at the in-plane angle. The solid lines represent a $\sin^2$ fit.

4. Magnon scattering on a pinned domain wall

In this section, we establish the model of a pinned domain wall. From the static properties of a pinned 180° domain wall, we then derive the equations of magnon scattering in an antiferromagnetic domain wall, which lead to the magnon reflection coefficient given in Eq. (1) of the main text.

A. Model of a Pinned Domain Wall

The dynamics of the space (**r**) distribution of the Néel vector **n**(**r**, *t*) (|**n**|=1) in an antiferromagnetic texture is described within the Lagrange formalism [13,14]. The Lagrange function is,

$$\mathcal{L} = \frac{M_s}{2\gamma^2 H_{ex}}[(\boldsymbol{n}\times\dot{\boldsymbol{n}} - \gamma\boldsymbol{H})^2 - c^2(\boldsymbol{n}\times\nabla\boldsymbol{n})^2] - w_{an}(\boldsymbol{n},\boldsymbol{H}) - w_{pin}(\boldsymbol{n},\boldsymbol{r}). \quad (S1)$$

Here, H_{ex} is the exchange field which characterizes the inter-sublattice coupling, γ is the gyromagnetic ratio, *c* is the magnon phase velocity and $M_s/2$ is the saturation magnetization of the magnetic sublattices. The density of the magnetic anisotropy is modelled according to the rhombohedral symmetry of hematite as,

$$w_{an} = -\frac{1}{2}M_s H_{2||}\cos^2\theta - \frac{1}{6}M_s H_{\perp}\sin^6\theta\cos 6\phi, \quad (S2)$$

here we use a parameterization of the Néel vector in terms of the spherical angles θ and φ where θ is the angle between ***n*** and the easy-axis and φ is the angle between ***n*** and some crystallographic direction perpendicular to the easy-axis. $H_{2||}(H) > 0$ can be treated as the effective uniaxial anisotropy field which incorporates the effects of both the DMI and the external magnetic field **H**$\|\hat{z}$ where $\hat{z}$ is the direction of the uniaxial anisotropy. A small in-plane anisotropy field $H_{\perp} > 0, H_{\perp} \ll H_{2||}$ is introduced in order to fix the orientation of the domain wall plane (the plane in which the Néel vector rotates).

We assume that the pinning of the domain wall originates from defects homogeneously distributed within the small interval $2x_{def}$ close to the domain wall center. The effective field of these defects, H_{pin}, favors an in-plane orientation of the Néel vector. The simplest form of such a pinning potential is,

$$w_{pin} = -\frac{1}{2}f(\xi)M_s H_{pin} x_{def}\sin^2\theta\cos^2\phi\,, \quad (S3)$$

where ξ is a coordinate in the direction of the domain wall normal and the form-function,

$f(\xi)$, is approximated with the Gaussian function as,

$$f(\xi) = \frac{1}{\sqrt{2\pi}x_{def}}\exp\left(-\frac{\xi^2}{2x_{def}^2}\right). \quad (S4)$$

Dynamic equations for the variables θ and φ are obtained from the Euler-Lagrange equations

with the Lagrange function (S1),

$$\ddot{\theta} - c^2\theta'' + \gamma^2 H_{ex}H_{2||}\sin\theta\cos\theta = \gamma^2 H_{ex}H_{pin}x_{def}f(\xi)\sin\theta\cos\theta\cos^2\phi\,, \qquad (S5)$$

$$\frac{d}{dt}\left(\dot{\phi}\sin^2\theta\right) - c^2(\phi'\sin^2\theta)' + \gamma^2 H_{ex}H_{\perp}\sin^6\theta\sin 6\phi = \gamma^2 H_{ex}H_{pin}x_{def}f(\xi)\sin^2\theta\cos\phi,$$

where $'$ indicates the spatial derivative in the ξ direction. In the first of equations (S5), we neglect the in-plane anisotropy term, $H_{\perp}$.

B. The Static Domain Wall

If the space distribution of the defects is much narrower that the domain wall width $x_{\mathrm{DW}} \equiv c/\left(\gamma\sqrt{H_{\mathrm{ex}}H_{2||}}\right)$, so that $x_{def} \ll x_{DW}$, equations (S5) are satisfied by the static solution,

$$\theta_0(\xi) = -\arctan\frac{1}{\sinh(\xi/x_{\mathrm{DW}})}, \quad \varphi_0 = 0, \qquad (S6)$$

which corresponds to a 180° domain wall with θ_0 varying from 0 to π. However, the energy (per unit squared) of the pinned domain wall depends on the distance X between the center of the domain wall and the point of the localization of the defects,

$$U(X) = E_{\mathrm{DW}} - \frac{x_{\mathrm{def}}M_s H_{\mathrm{pin}}}{2\cosh^2(X/x_{\mathrm{DW}})}, \qquad (S7)$$

where $E_{\mathrm{DW}} = 2x_{\mathrm{DW}}M_s H_{2||}$ is the domain wall energy in the absence of pinning. Expression (S7) is calculated under the assumption that $\theta = \theta_0(\xi - X)$. The value of $E_{\mathrm{pin}} = x_{\mathrm{def}}M_s H_{\mathrm{pin}}/2$ can be associated with the pinning energy.

C. Magnon transport across a domain wall

Having established a model for a pinned domain wall, we now turn our attention to the interaction between an incident magnon and the domain wall. The magnons in the domain wall are the perturbations of the Néel vector on top of the static solution given in equation (S6). Using the ansatz $\theta = \theta_0(\xi) + \tilde{\theta}(t), \varphi = \varphi_0 + \tilde{\chi}(t)/\sin^2\theta_0$, where $\tilde{\theta}(t), \tilde{\chi}(t) \propto e^{i\omega t}$ represent the perturbation from the equilibrium state, we reduce equations (S5) to a standard 1D Schrödinger-like problem (see e.g. Reference [15]),

$$\hat{\mathcal{H}}_0\tilde{\theta} - \frac{H_{\text{pin}}}{H_{2||}} x_{\text{def}} f(\xi) \cos 2\,\theta_0 \tilde{\theta} = \varepsilon\tilde{\theta}, \qquad (S8)$$

$$-x_{\text{DW}}^2\tilde{\chi}'' - \frac{H_{\text{pin}}}{H_{2||}} x_{\text{def}} f(\xi)\tilde{\chi} = \varepsilon\tilde{\chi},$$

where $\varepsilon = \omega^2/\left(\gamma^2 H_{\text{ex}} H_{2||}\right)$ is the dimensionless magnon energy and

$$\hat{\mathcal{H}}_0 = -x_{\text{DW}}^2 \frac{d^2}{d\xi^2} + 1 - \frac{2}{\cosh^2(\xi/x_{\text{DW}})}, \qquad (S9)$$

is the Hamilton operator with a Pöschl-Teller potential (which is reflectionless)[16,17]. The in-plane anisotropy is neglected as compared to the pinning potential ($H_\perp \ll H_{pin}$). We also assumed that H=0.

In the limit $x_{def} \ll x_{DW}$, the second of equations (S8) is a well-known Schrödinger equation with a delta function potential. The first of equations (S8) also reduces to the Schrödinger equation with a delta potential shifted by -E_{pin} due to the supersymmetry of the operator given in equation (S9) (for details of the technique, see reference [18]). Such a potential leads to the reflection of incident plane waves $\tilde{\theta}(t)$, $\tilde{\chi}(\text{t}) \propto e^{i\omega t - ik\xi}$ with a reflection coefficient given in the main text as Eq. (1).

5. Comparison of domain sizes from PEEM images

Table 1 shows a summary of the domain sizes, domain wall widths and extracted diffusion lengths from electrical transport measurements. Supplementary Figure S7 shows example profiles of the intensity squared through PEEM images of both (0001) orientated films in the easy-plane phase and the $(1\bar{1}02)$ orientated films at 100 K in the easy-axis phase. The domain walls and domains are indicated. The domain wall widths were defined by where the intensity reached 25% and 75% of the difference between domains for the (0001) orientated films and at 25% intensity for the $(1\bar{1}02)$ orientated films.

One can notice that the scattering length dominates the magnon decay only when the average size of the antiferromagnetic domains is smaller than the intrinsic diffusion length of the magnons.

Film Orientation	Domain Size (nm)	Domain Wall Width (nm)	Intrinsic diffusion Length λ_0 (nm)	Scattering Length λ_1 (nm)
Measurement technique	XMLD-PEEM	XMLD-PEEM	Electrical transport	Electrical transport
$(1\bar{1}02)$	2230±930	147±23	700±100	$>>\lambda_0$
(0001) ($T>T_M$)	485±225	79±32	700±50	67±10
(0001) ($T<T_M$)	460±205	105±25	350±30	$>>\lambda_0$

Table 1: Domain size and domain wall width for 500 nm $(1\bar{1}02)$ orientated hematite films and 100nm (0001) orientated hematite in both the easy-axis ($T<T_M$, $H<H_{c,sf}^{||}$) and easy-plane phases ($T>T_M$, $H>H_{c,sf}^{||}$). The resulting diffusion lengths from fitting electrical transport data is included for comparison. The error bars, representing the standard deviation in the average sizes, is determined by the lack of statistics arising from the size of the XMLD-PEEM images.

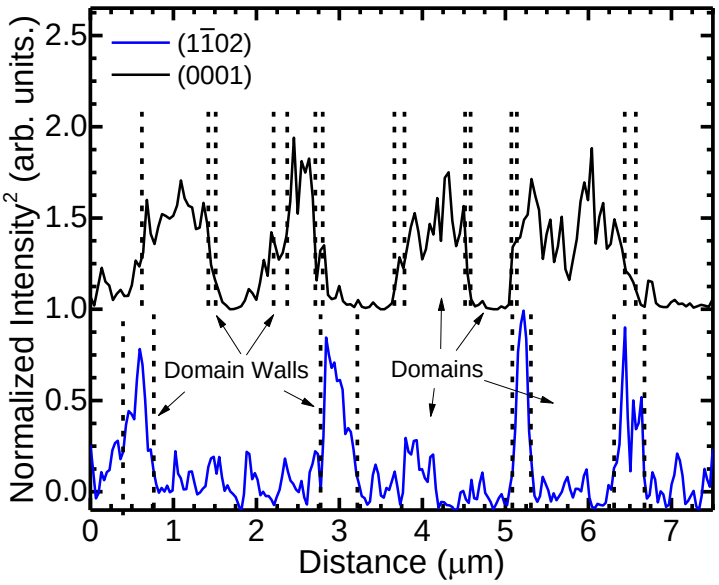

Supplemental Figure S7 Intensity profiles of XMLD-PEEM images of (0001) and (1$\bar{1}$02) orientated hematite films. The (0001) intensity profile is from the easy-plane phase whilst the (1$\bar{1}$02) was taken in the easy-axis phase.

(1) Momma, K.; Izumi, F. VESTA : A Three-Dimensional Visualization System for Electronic and Structural Analysis. *J. Appl. Crystallogr.* **2008**, *41* (3), 653–658.

(2) Grave, D. A.; Dotan, H.; Levy, Y.; Piekner, Y.; Scherrer, B.; Malviya, K. D.; Rothschild, A. Heteroepitaxial Hematite Photoanodes as a Model System for Solar Water Splitting. *J. Mater. Chem. A* **2016**, *4* (8), 3052–3060.

(3) Appel, P.; Shields, B. J.; Kosub, T.; Hedrich, N.; Hübner, R.; Faßbender, J.; Makarov, D.; Maletinsky, P. Nanomagnetism of Magnetoelectric Granular Thin-Film Antiferromagnets. *Nano Lett.* **2019**, *19* (3), 1682–1687.

(4) Morin, F. J. Magnetic Susceptibility of α-Fe2O3 and α-Fe2O3 with Added Titanium. *Phys. Rev.* **1950**, *78* (6), 819–820.

(5) Pati, S. P.; Al-Mahdawi, M.; Ye, S.; Nozaki, T.; Sahashi, M. Control of Spin-Reorientation Transition in (0001) Oriented α-Fe2O3 Thin Film by External Magnetic Field and Temperature. *Phys. status solidi - Rapid Res. Lett.* **2017**, *11* (7), 1700101.

(6) Shimomura, N.; Pati, S. P.; Sato, Y.; Nozaki, T.; Shibata, T.; Mibu, K.; Sahashi, M. Morin Transition Temperature in (0001)-Oriented α-Fe 2 O 3 Thin Film and Effect of Ir Doping. *J. Appl. Phys.* **2015**, *117* (17), 17C736.

(7) Artman, J. O.; Murphy, J. C.; Foner, S. Magnetic Anisotropy in Antiferromagnetic Corundum-Type Sesquioxides. *Phys. Rev.* **1965**, *138* (3A), A912–A917.

(8) Cornelissen, L. J.; Liu, J.; Duine, R. A.; Youssef, J. Ben; Van Wees, B. J. Long-Distance Transport of Magnon Spin Information in a Magnetic Insulator at Room Temperature. *Nat. Phys.* **2015**, *11* (12), 1022–1026.

(9) Lebrun, R.; Ross, A.; Bender, S. A.; Qaiumzadeh, A.; Baldrati, L.; Cramer, J.; Brataas, A.; Duine, R. A.; Kläui, M. Tunable Long-Distance Spin Transport in a Crystalline Antiferromagnetic Iron Oxide. *Nature* **2018**, *561* (7722), 222–225.

(10) Morrison, B. R.; Morrish, A. H.; Troup, G. J. High-Field Antiferromagnetic Resonance in α-Fe2O3. *Phys. Status Solidi* **1973**, *56* (1), 183–195.

(11) Ganzhorn, K.; Wimmer, T.; Cramer, J.; Schlitz, R.; Geprägs, S.; Jakob, G.; Gross, R.; Huebl, H.; Kläui, M.; Goennenwein, S. T. B. Temperature Dependence of the Non-Local Spin Seebeck Effect in YIG/Pt Nanostructures. *AIP Adv.* **2017**, *7* (8), 085102.

(12) Gurevich, A. G.; Melkov, G. A. *Magnetization Oscillations and Waves*; CRC Press, 1996.

(13) Kosevich, A. M.; Ivanov, B. A.; Kovalev, A. S. Magnetic Solitons. *Phys. Rep.* **1990**, *194* (3–4), 117–238.

(14) Gomonay, E. V.; Loktev, V. M. Spintronics of Antiferromagnetic Systems (Review Article). *Low Temp. Phys.* **2014**, *40* (1), 17–35.

(15) Ivanov, B. A.; Sukstanskii, A. L. On Magnetic Relaxation in Antiferromagnets. *J. Magn. Magn. Mater.* **1992**, *117* (1–2), 102–118.

(16) Tveten, E. G.; Qaiumzadeh, A.; Brataas, A. Antiferromagnetic Domain Wall Motion Induced by Spin Waves. *Phys. Rev. Lett.* **2014**, *112* (14), 147204.

(17) Qaiumzadeh, A.; Kristiansen, L. A.; Brataas, A. Controlling Chiral Domain Walls in Antiferromagnets Using Spin-Wave Helicity. *Phys. Rev. B* **2018**, *97* (2), 020402.

(18) Cooper, F.; Khare, A.; Sukhatme, U. Supersymmetry and Quantum Mechanics. *Phys. Rep.* **1995**, *251* (5–6), 267–385.